

Low- x QCD with CMS at the LHC

David d'Enterria¹ for the CMS collaboration

¹CERN, PH-EP, CH-1211 Geneva 23, Switzerland

Received: date / Revised version: date

Abstract. The physics of gluon saturation and non-linear evolution at small values of parton momentum fraction x in the proton and nucleus is discussed in the context of experimental results at HERA and RHIC. The rich physics potential of low- x QCD studies at the LHC is discussed and some measurements in pp, pA and AA collisions accessible with the Compact Muon Solenoid (CMS) experiment are presented.

PACS. 12.38.-t – 24.85.+p – 25.75.-q

1 Introduction

1.1 Parton structure and evolution

Deep inelastic scattering (DIS) electron-proton ep (and electron-nucleus, eA) collisions provide a precise means to study the partonic structure of the proton (and nucleus). The inclusive DIS hadron cross section, $d^2\sigma/dx dQ^2$, is a function of the virtuality Q^2 of the exchanged gauge boson (i.e. its “resolving power”), and the Bjorken- x fraction of the total nucleon momentum carried by the struck parton. The differential cross section for the neutral-current (γ/Z exchange) process is written in terms of the target structure functions as

$$\frac{d^2\sigma}{dxdQ^2} = \frac{2\pi\alpha^2}{xQ^4} Y_+ F_2 Y_- xF_3 \bar{y}^2 \bar{l}F ; \quad (1)$$

where $Y = 1 - (1 - y)^2$ is related to the inelasticity y of the collision, and the structure functions $F_{2,3,L}(x;Q^2)$ describe the density of quarks and gluons in the hadron¹. F_2 is the dominant contribution to the cross section over most of phase space. One of the most significant discoveries at HERA is the strong growth of the inclusive DIS cross section for decreasing Bjorken- x at fixed Q^2 as well as for increasing Q^2 at fixed x (Fig. 1). The strong scaling violations evident at small x in Fig. 1 are indicative of the increasing gluon radiation. At small x , F_2 is sensitive to the sea quark distribution, driven by the gluon splitting, and since

$$\partial F_2(x=2;Q^2) = \partial \ln Q^2 \propto \alpha_s(Q^2) x g(x;Q^2) ; \quad (2)$$

the gluon density $x g(x;Q^2)$ can be thus determined (Fig. 2). Once measured at an input scale $Q_0^2 \gtrsim 2 \text{ GeV}^2$, the parton distribution functions (PDFs) at any other Q^2 are given by the Dokshitzer-Gribov-Lipatov-Altarelli-Parisi (DGLAP) evolution equations which govern the probability of parton branchings (gluon splitting, $q;g \rightarrow q;g$ strahlung) in QCD [2].

¹ $F_2 \propto e_q^2 x \sum_i (q_i + \bar{q}_i)$, $x F_3 \propto x \sum_i (q_i - \bar{q}_i)$, $F_L \propto \alpha_s x g$.

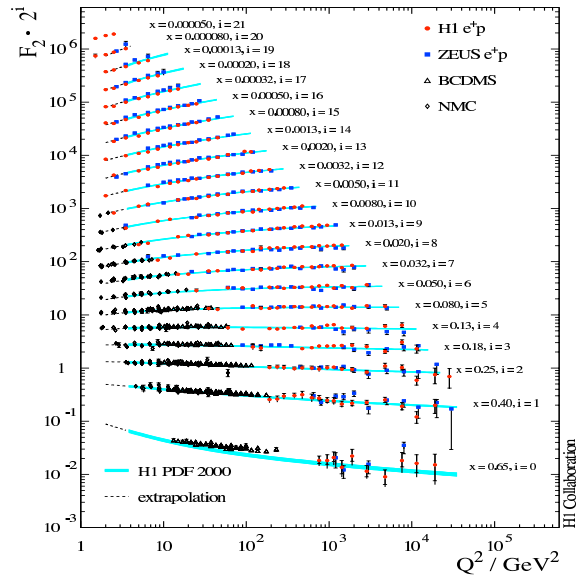


Fig. 1. $F_2(x;Q^2)$ measured in DIS at HERA and fixed-target experiments.

The DGLAP parton evolution, however, only takes into account the Q^2 -dependence of the PDFs, resumming over single logarithms in $\alpha_s \ln(Q^2)$, “leading twist”, but neglecting the $1=x$ terms. At large energies (small x), the probability of emitting an extra gluon increases as $\propto \alpha_s \ln(1=x)$. In this regime, the evolution of parton densities proceeds over a large rapidity region, $\Delta y \propto \ln(1=x)$, and the finite transverse momenta of the partons become increasingly important. Thus, their appropriate description is in terms of k_T -unintegrated PDFs, $x g(x; k_T)$, described by the Balitski-Fadin-Kuraev-Lipatov (BFKL) equation which governs parton evolution in x at fixed Q^2 [3]. Hints of extra BFKL radiation have been recently found in the enhanced production of forward jets at HERA compared to DGLAP expectations [4, 5].

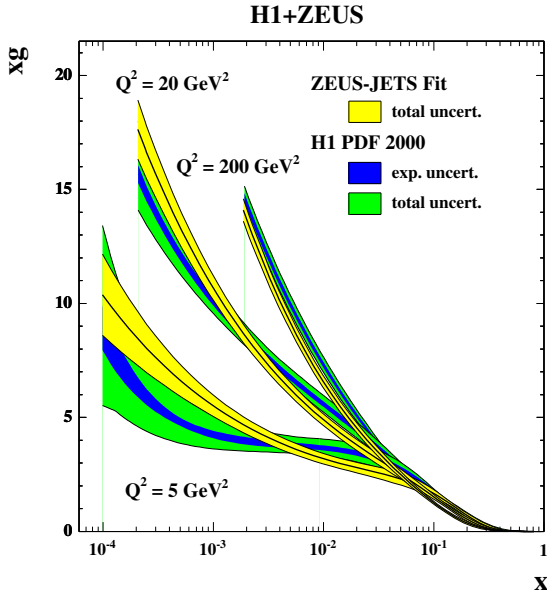


Fig. 2. Gluon distributions extracted at HERA (H1 and ZEUS) as a function of x in three bins of Q^2 [1].

1.2 Parton saturation and non-linear evolution at low x

As shown in Figures 1 and 2, the gluon density rises very fast for decreasing x . For $x < 0.01$, the growth in F_2 is well described by $F_2(x; Q^2) \propto x^{-\lambda(Q^2)}$ with $\lambda = 0.1 - 0.3$ logarithmically rising with Q^2 [6]. Eventually, at some small enough value of x one expects to enter a regime where the gluon density becomes so large that non-linear (gg fusion) effects become important, taming the growth of the parton densities. In such a high-gluon density regime three things are expected to occur: (i) the standard DGLAP and BFKL *linear* equations should no longer be applicable since they only account for single parton branchings (1 ! 2 processes) but not for non-linear (2 ! 1) gluon recombination; (ii) pQCD (collinear and k_T) factorization should break due to its (now invalid) assumption of *incoherent* parton scattering; and, as a result, (iii) standard pQCD calculations lead to a *violation of unitarity* even for $Q^2 < \Lambda^2$. Figure 3 schematically depicts the different domains of the parton density as a function of $y = \ln(1-x)$ and Q^2 . The transition to the regime of saturated PDFs is expected for small x values below an energy-dependent ‘saturation momentum’, Q_s , intrinsic to the (size of the) hadron. Since $xG(x; Q^2)$ can be interpreted as the number of gluons with transverse area $r^2 = 1/Q^2$ in the hadron wavefunction, an increase of Q^2 effectively diminishes the ‘size’ of each parton, partially compensating for the growth in their number (i.e. the higher Q^2 is, the smaller the x at which saturation sets in). Saturation effects are, thus, expected to occur when the size occupied by the partons becomes similar to the size of the hadron, πR^2 . This provides a definition for the saturation scale of an arbitrary hadron with A nucleons (i.e. with gluon density $xG = A - xg$):

$$Q_s^2(x) \propto \alpha_s \frac{1}{\pi R^2} xG(x; Q^2) \propto A^{1/3} x^{-\lambda} \propto A^{1/3} \left(\frac{P}{s}\right)^{\lambda} \propto A^{1/3} e^{\lambda y}; \quad (3)$$

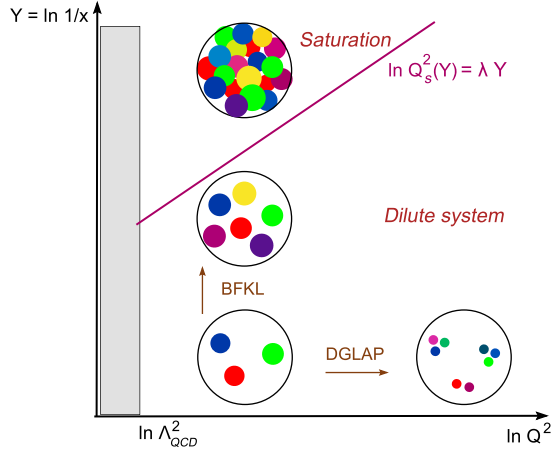


Fig. 3. QCD ‘phase diagram’ in the $1-x; Q^2$ plane (each dot represents a parton with transverse area $1=Q^2$ carrying a fraction x of the hadron momentum) [7].

with $\lambda = 0.25$ [8]. Equation (3) indicates that Q_s grows with the number of nucleons, A , of the target, and the energy of the collision, P/\bar{s} , or equivalently, the rapidity of the gluon $y = \ln(1-x)$. The mass number, A , dependence implies that, at equivalent energies, saturation effects will be enhanced by factors as large as $A^{1/3} \approx 6$ in heavy nuclear targets ($A = 208$ for Pb) compared to protons. In the last fifteen years, an effective field theory of QCD in the high-energy (high density, small x) limit has been developed - the Colour Glass Condensate (CGC) [9] - which describes the hadrons in terms of classical fields (saturated gluon wavefunctions) below the saturation scale Q_s . The saturation momentum Q_s introduces a (semi-)hard scale, $Q_s \approx \Lambda$, which not only serves as an infrared cut-off to unitarize the cross sections but allows weak-coupling perturbative calculations ($\alpha_s(Q_s) \ll 1$) in a strong $F_{\mu\nu}$ colour field background. Hadronic and nuclear collisions are seen as collisions of classical wavefunctions which ‘resum’ all gluon recombinations and multiple scatterings. The quantum evolution in the CGC approach is given by the JIMWLK [10] non-linear equations (or by their mean-field limit for $N_c \rightarrow \infty$, the Balitsky-Kovchegov equation [11]) which reduce to the standard BFKL kernel at higher x values.

2 Parton saturation: Experimental studies

The main source of information on the *quark* densities is obtained from measurements of (i) the structure functions $F_{2,3}$ in lepton-hadron scattering, and (ii) lepton pair (Drell-Yan) production in hadron-hadron collisions. The *gluon* densities, xG enter at LO directly in hadron-hadron scattering processes with (i) prompt photons and (ii) jets in the final state, as well as in the (difficult) measurement of (iii) the longitudinal DIS structure function F_L (and also indirectly in F_2 through the derivative in Eq. (2)). In addition, (iv) heavy vector mesons ($J/\psi; \Upsilon$) from diffractive photoproduction processes² are a valuable probe of the gluon density since their cross sections are proportional to

² Diffractive γp (γA) processes are characterized by a quasi-elastic interaction - mediated by a Pomeron or two gluons in a colour singlet

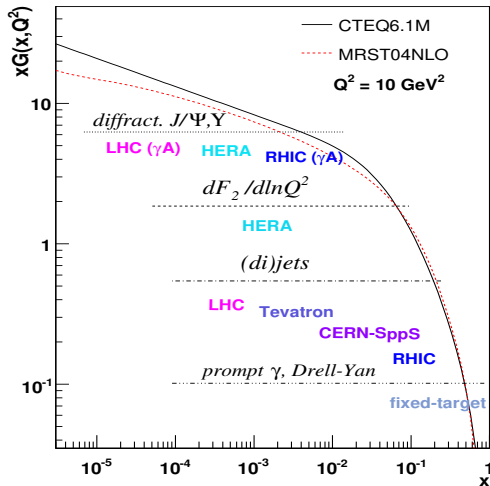


Fig. 4. Experimental measurements at various facilities providing information on the gluon PDF in different ranges of Bjorken- x .

the *square* of xG [12, 13]:

$$\frac{d\sigma_{\gamma p \rightarrow A \rightarrow V p \rightarrow A}}{dt} \Big|_{t=0} = \frac{\alpha_s^2 \Gamma_{ee}}{3\alpha M_V^5} 16\pi^3 \ x G(x; Q^2)^2; \quad (4)$$

with $Q^2 = M_V^2 = 4$ and $x = M_V^2/W_{\gamma p;A}^2$: (5)

In hadronic collisions, one commonly measures (real and virtual) photons and jets at central rapidities ($y = 0$) where $x = Q^2 / s$, with $Q = 2p_T \cdot M$ the typical scale of the produced particle. However, one can probe smaller x values in the target by measuring the corresponding cross sections in the *forward* direction. Indeed, since for a $2 \rightarrow 2$ process³

$$x_{1,2} = \frac{p}{s} (e^{-y_1} + e^{-y_2}); \quad (6)$$

x decreases by a factor of 10 every two units of rapidity.

Figure 4 summarizes the range of experimental processes sensitive to the gluon density and their approximate x coverage. Figure 5 shows the kinematical map in $(x; Q^2)$ of the DIS, DY, direct γ and jet data used in the PDF fits. Results from HERA and the Tevatron cover a substantial range of the proton structure ($10^{-4} \lesssim x \lesssim 0.8$, $1 \lesssim Q^2 \lesssim 10^5$ GeV 2) but the available measurements are much rarer in the case of nuclear targets (basically limited to fixed-target studies, $10^{-2} \lesssim x \lesssim 0.8$ and $1 \lesssim Q^2 \lesssim 10^2$ GeV 2). As a matter of fact, the nuclear parton distributions are basically unknown at low x ($x < 0.01$) where the only available measurements are fixed-target data in the *non-perturbative* range ($Q^2 < 1$ GeV 2) dominated by Regge dynamics rather than quark/gluon degrees of freedom. An example of the current lack of knowledge of the nuclear densities at low x is presented in Fig. 6 where different available parametrizations of the ratio of Pb to proton gluon distributions, consistent with the available nDIS data at higher x , show differences as large as a factor of three [18].

state - in which the p (A) remains intact (or in a low excited state) and separated by a rapidity gap from the rest of final-state particles.

³ The allowed x can be much lower for non-linear 2 ! 1 processes in which the momentum is “balanced” by the medium [14].

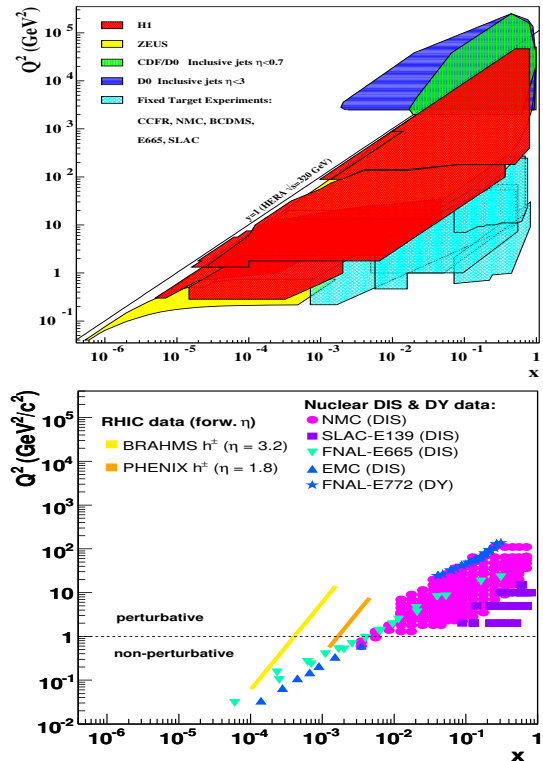


Fig. 5. Available measurements in the (x, Q^2) plane used for the determination of the proton [15] (top) and nuclear [16] (bottom) PDFs.

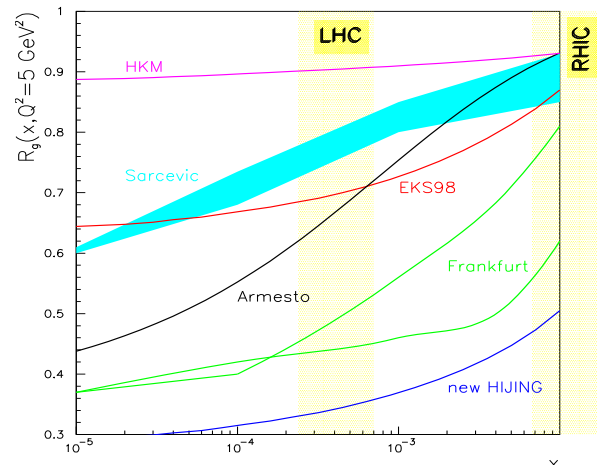


Fig. 6. Ratios of the Pb over proton gluon PDFs versus x from different models at $O^2 = 5 \text{ GeV}^2$. Figure taken from [17].

2.1 HERA results

Though the large majority of ep DIS data collected during the HERA-I phase are consistent with standard DGLAP predictions, more detailed and advanced experimental and theoretical results in the recent years have pointed to interesting hints of non-linear QCD effects in the data. Arguably, the strongest manifestation of such effects is given by the so-called “geometric scaling” property observed in inclusive σ_{DIS}

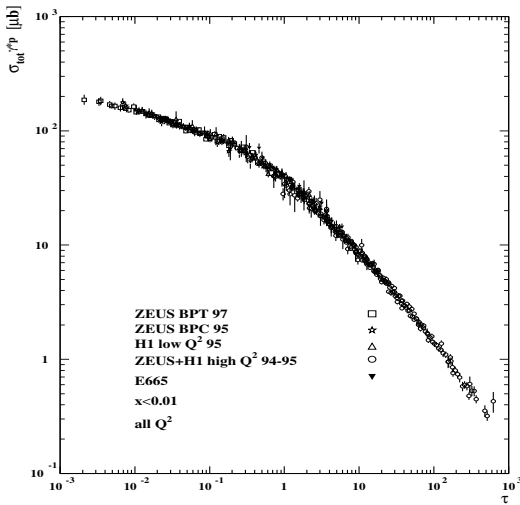


Fig. 7. Geometric scaling in the DIS $\gamma^2 p$ cross sections plotted versus $\tau = Q^2/Q_s^2$ in the range $x < 0.01$, $0.045 < Q^2 < 450$ GeV 2 [19].

for $x < 0.01$ [19] as well as in various diffractive cross sections [20, 21]. For inclusive DIS events, this feature manifests itself in a total cross section at small x ($x < 0.01$) which is only a function of $\tau = Q^2/Q_s^2(x)$, instead of being a function of x and Q^2/Q_s^2 separately (Fig. 7). The saturation momentum follows $Q_s(x) = Q_0(x=x_0)^\lambda$ with parameters $\lambda = 0.3$, $Q_0 = 1$ GeV, and $x_0 = 3 \cdot 10^{-3}$. Interestingly, the scaling is valid up to very large values of τ , well above the saturation scale, in an “extended scaling” region with $Q_s^2 < Q^2 < Q_s^4 = \Lambda_{QCD}^2$ [22, 7]. The saturation formulation is suitable to describe not only inclusive DIS, but also inclusive diffraction $\gamma^2 p \rightarrow X p$. The very similar energy dependence of the inclusive diffractive and the total cross section in $\gamma^2 p$ collisions at a given Q^2 is easily explained in the Golec-Biernat Wüsthoff model [19] but not in standard collinear factorization. Furthermore, geometric scaling has been also found in different diffractive DIS cross sections (inclusive, vector mesons, DVCS) [20, 21]. All these results suggest that the observed scalings are indeed manifestations of the saturation regime of QCD. Unfortunately, the value of $Q_s = 1$ GeV at HERA lies in the transition region between the soft and hard sectors and, therefore, non-perturbative effects obscure the obtention of clearcut experimental signatures.

2.2 RHIC results

The expectation, based on Eq. (3), of enhanced parton saturation effects in the nuclear wave functions accelerated at ultra-relativistic energies has been one of the primary physics motivations for the heavy-ion programme at RHIC⁴ [9]. Further, the properties of the high-density matter produced in the final-state of AA interactions cannot be properly interpreted without having determined the influence of *initial state* modifications of the nuclear PDFs. In this context, after five years of operation, two main experimental observations at RHIC have been found

⁴ The saturation scale at $y=0$ in Au at RHIC is $Q_s^2 = 2$ GeV, much larger than that of protons probed at HERA, $Q_s^2 = 0.5$ GeV.

consistent with CGC predictions: (i) the modest hadron multiplicities measured in AuAu reactions, and (ii) the suppressed hadron yield at forward rapidities in dAu collisions.

The bulk, $dN_{ch}=d\eta \int_{\eta=0}^{\eta=0.7} d\eta$, multiplicities measured at mid-rapidity in central AuAu at $\sqrt{s_{NN}} = 200$ GeV are comparatively lower than the $dN_{ch}=d\eta \int_{\eta=0}^{\eta=0.7} d\eta$, 1000 predictions [23] of “minijet” scenarios, soft Regge models, or extrapolations from an incoherent sum of proton-proton collisions, but they can be reproduced by approaches based on gluon saturation [8, 24] which take into account a reduced parton flux in the nuclear targets, i.e. $f_{a=A}(x;Q^2) < A \int_{x_a}^A f_N(x;Q^2)$. In the CGC calculations, the final hadron multiplicities are assumed to be simply related to the initial number of released partons (local parton-hadron duality) which are depleted in the initial state compared to pp collisions due to non-linear gluon-gluon recombinations [8]. Simple assumptions related to the dependence of the saturation scale on energy and overlapping area of the colliding nuclei, describe the centrality and center-of-mass (c.m.) energy dependences of the bulk AA hadron production (Fig. 8).

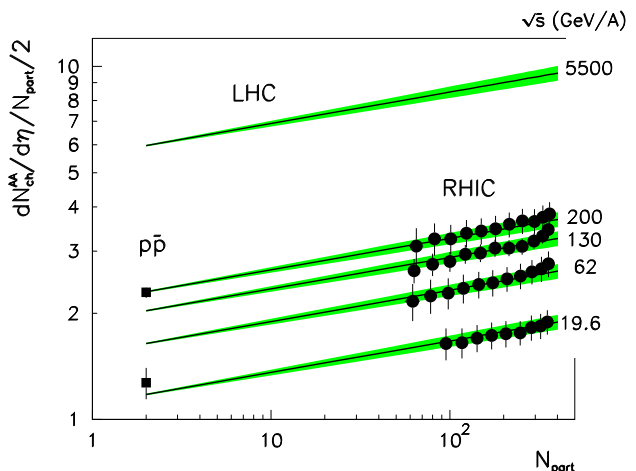


Fig. 8. Dependences on c.m. energy and centrality (given in terms of the number of nucleons participating in the collision, N_{part}) of $dN_{ch}=d\eta \int_{\eta=0}^{\eta=0.7} d\eta$ (normalized by N_{part}): PHOBOS AuAu data [25] vs the predictions of the saturation approach [24].

The second manifestation of saturation-like effects in the RHIC data is the BRAHMS observation [26] of suppressed yields of moderately high- p_T hadrons ($p_T = 2 - 4$ GeV/c) in dAu relative to pp collisions at $\eta = 3.2$. Hadron production at such small angles is sensitive to partons in the Au nucleus with $x \sim 0.10^{-3}$. The observed nuclear modification factor, $R_{dAu} \sim 0.8$, cannot be reproduced by pQCD calculations that include standard *leading-twist* shadowing of the nuclear PDFs [14, 27] but can be described by CGC approaches [28] that parametrize the Au nucleus as a saturated gluon wavefunction. In addition, a recent analysis of the nuclear DIS F_2 data also confirms the existence of “geometrical scaling” for $x < 0.017$ [24].

3 Low- x QCD at the LHC

The Large Hadron Collider (LHC) at CERN will provide pp, pA and AA collisions at $\sqrt{s_{NN}} = 14, 8.8$ and 5.5 TeV respec-

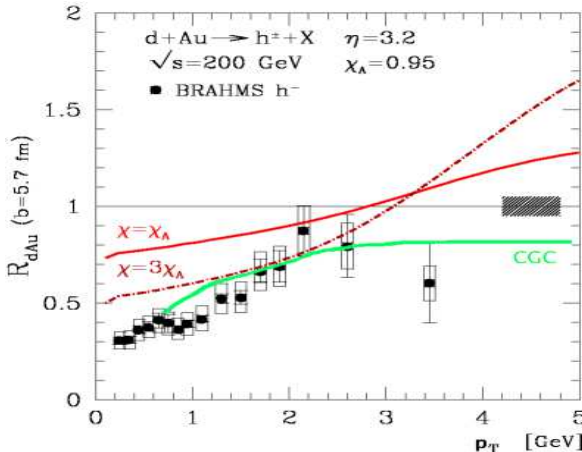


Fig. 9. Nuclear modification factor R_{dAu} (p_T) for charged hadrons produced in dAu at $\sqrt{s_{NN}} = 200$ GeV: BRAHMS data [26] versus DGLAP shadowing [14] and CGC [28] predictions. Fig. adapted from [14].

tively with luminosities $L = 10^{34}, 10^{29}$ and $5 \cdot 10^{26} \text{ cm}^{-2} \text{ s}^{-1}$. Such large c.m. energies and luminosities will allow detailed QCD studies at unprecedented low x values thanks to the copious production of hard probes (jets, quarkonia, prompt γ , Drell-Yan pairs, etc.). The expected advance in the study of low- x QCD phenomena will be specially substantial for nuclear systems since the saturation momentum, Eq. (3), $Q_s^2 = 5 - 10 \text{ GeV}^2$, will be in the perturbative range [8], and the relevant x values, Eq. (6), will be 30–70 times lower than AA and pA reactions at RHIC: $x = 10^{-3}$ (10^{-5}) at central (forward) rapidities for processes with $Q^2 = 10 \text{ GeV}^2$ (Fig. 10).

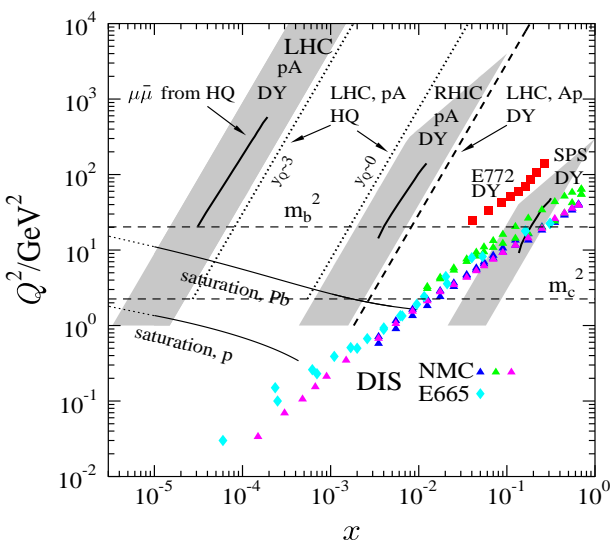


Fig. 10. Kinematical ($x; Q^2$) range probed at various rapidities y and c.m. energies in $\sqrt{s_{NN}} = 8.8 \text{ TeV}$ pA collisions at the LHC [17].

3.1 The CMS experiment

The CMS experiment is one of the two large general-purpose detectors being installed at the LHC. Its experimental capabili-

ties are extremely well adapted for the study of low- x phenomena with proton and ion beams featuring:

- (i) Very large acceptance at midrapidity ($|\eta| < 2.5$, full ϕ) for charged and neutral hadrons as well as μ^+ , e^+ , and γ over a wide range of p_T (the 4 T magnetic field results in the best track momentum resolution at LHC).
- (ii) Excellent muon reconstruction leading to the best mass resolution for J/ψ , and Υ measurements at the LHC.
- (iii) Complete electromagnetic (EM) and hadronic (HAD) calorimetry for full jet reconstruction over $|\eta| < 3$ and $\Delta\phi = 2\pi$ with a large statistical significance for single jet and jet+ X ($X = \text{jet}, \gamma, Z$) channels.
- (iv) Unparalleled forward physics capabilities thanks to the forward hadronic calorimeter (HF, $3 < |\eta| < 5$), TOTEM T1 ($3.1 < |\eta| < 4.7$) and T2 ($5.5 < |\eta| < 6.6$) trackers, and CASTOR ($5.3 < |\eta| < 6.7$) and zero-degree (ZDC, $|\eta| > 8.1$ for neutrals) calorimeters.

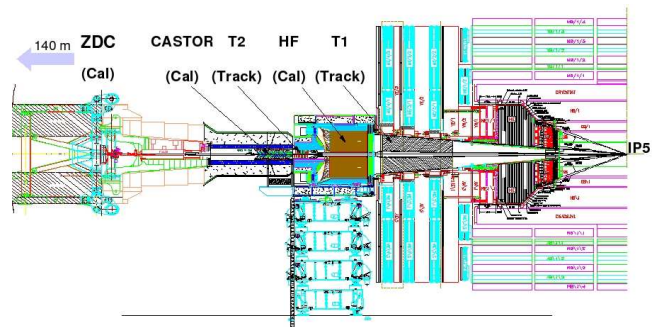


Fig. 11. Layout of the detectors in the CMS forward region.

The combination of HF, TOTEM, CASTOR and ZDC (Fig. 11) makes of CMS the largest acceptance detector ever built at a hadron collider. The HF [29], located 11.2 m away on both sides of the interaction point (IP), is a steel plus quartz-fiber Čerenkov calorimeter with 1200 channels ($\Delta\eta = 0.18$, $\Delta\phi = 0.18$, 1.65 m absorber corresponding to 10.3λ) sensitive to the deposited EM and HAD energy, allowing jet reconstruction at very forward rapidities. The T1 and T2 telescopes are part of the the TOTEM experiment [30] which shares the same IP as CMS and are mainly designed to measure charged tracks from diffractive dissociation processes. CASTOR [31] is an azimuthally symmetric electromagnetic/hadronic calorimeter situated at 14.37 m from the interaction point covering the same acceptance as T2. The calorimeter is a Čerenkov-light device, consisting of successive layers of tungsten absorber and fused silica (quartz) plates as active medium arranged in 2 EM (10 HAD) sections of about $22X_0$ ($10.3\lambda_I$) radiation (interaction) lengths. The ZDC [32] is also a tungsten+quartz sampling Čerenkov calorimeter with 5 EM ($19X_0$, divided in x) and 4 HAD ($5.6\lambda_I$, divided z) sections. It is located at 140 m from the CMS vertex at the end of the straight sections of the two LHC pipes containing the countercirculating beams. The purpose of the ZDC is to measure very forward going neutrons and photons with $\sim 10\%$ (2 mm) energy (position) resolution.

3.2 Low- x QCD measurements in CMS

The following three measurements in pp, pA and AA collisions are being considered in CMS to look for signatures of high gluon density effects at low x .

3.2.1 Forward jets (pp, pA, AA)

The cross section for dijet production in the forward direction, “Muller-Navelet jets” [33], is a particularly sensitive measure of the small x parton dynamics in hadronic collisions [5]. The two HF calorimeters ($3 < |\eta| < 5$), specifically designed to measure energetic forward jets⁵, have an energy resolution of 20% for typical jets with $E_T > 40$ GeV (i.e. $E = E_T \cosh \eta$ 1 TeV at $|\eta| = 4$). In the presence of low- x saturation effects, the forward-backward dijet production cross section (separated by $\Delta\eta = 9$ and, thus, measurable in each of the HFs) is expected to be suppressed by a factor of ~ 2 in pp at 14 TeV (Fig. 12). A study is underway to determine the feasibility of such measurements in CMS.

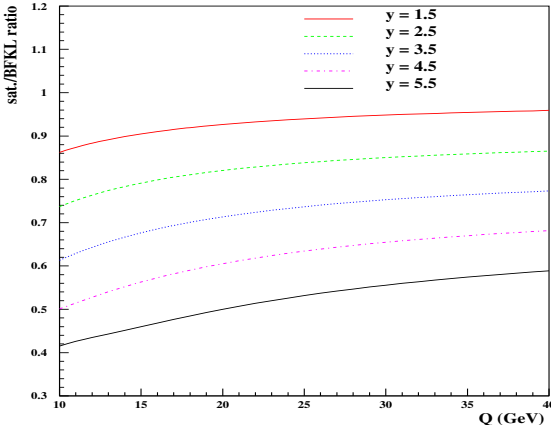


Fig. 12. Ratio of the saturation over BFKL predictions for the Müller-Navelet forward jet cross sections in pp collisions at $\tilde{P} \cdot \tilde{s} = 14$ TeV as a function of $Q = Q_1 = Q_2$ for different values of $y = y_1 = y_2$ [5].

3.2.2 $Q\bar{Q}$ photoproduction (electromagnetic AA collisions)

High-energy diffractive production of heavy vector mesons ($J/\psi; \Upsilon$) proceeds through colourless two-gluon exchange (which couples to $\gamma^* + Q\bar{Q}$) and is thus a sensitive probe of the low- x gluon densities, see Eq. (4). Ultra-peripheral interactions (UPCs) of high-energy heavy ions generate strong electromagnetic fields which help constrain the low- x behaviour of xG via quarkonia produced in γ -nucleus collisions [34]. Lead beams at 2.75 TeV have Lorentz factors $\gamma = 2930$ leading to maximum (equivalent) photon energies $\omega_{max} = \gamma R = 100$ GeV, and c.m. energies $W_{\gamma\gamma}^{max} = 160$ GeV and $W_{\gamma A}^{max} = 1$ TeV. From Eq. (5), the x values probed in $\gamma A + J/\psi A$ processes at $y = 2$ can be as

⁵ The HF plays a prominent role in forward jet tagging for the vector-boson-fusion ($qq + qqH$) Higgs production channel.

low as $x \sim 10^{-5}$. The CMS experiment can measure $\Upsilon + \mu^+ \mu^-$ produced in electromagnetic PbPb collisions tagged with neutrons detected in the ZDCs (as done at RHIC [34]). Figure 13 shows the expected dimuon invariant mass distributions predicted by STARLIGHT [35] within the CMS acceptance for an integrated PbPb luminosity of 0.5 nb^{-1} . An Υ peak with ~ 1200 counts is clearly seen on top of the $\mu^+ \mu^-$ continuum.

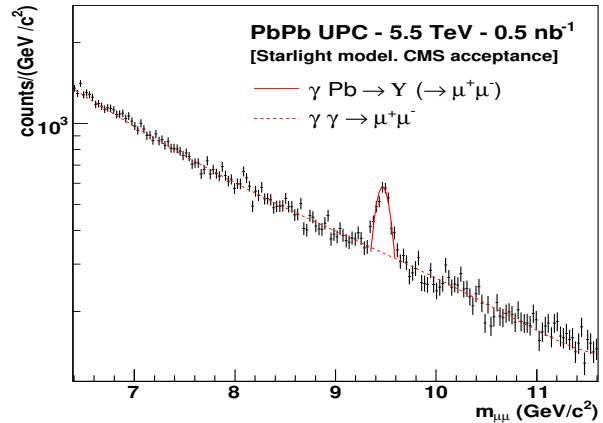


Fig. 13. Expected $\mu^+ \mu^-$ invariant mass from $\gamma Pb + Y Pb^2 + \mu^+ \mu^-$ and $\gamma \gamma + \mu^+ \mu^-$ as given by Starlight [35] for UPC PbPb collisions at $\tilde{P} \cdot \tilde{s}_{NN} = 5.5$ TeV in the CMS acceptance.

3.2.3 Forward Drell-Yan pairs (pp, pA, AA)

High-mass Drell-Yan pair production at the very forward rapidities covered by CASTOR and T2 ($|\eta| < 5 - 6$) can probe the parton densities down to $x \sim 10^{-6}$. A study is underway in CMS to combine the CASTOR electromagnetic energy measurement together with the good position resolution of T2 for charged tracks, to trigger on and reconstruct the $e^+ e^-$ invariant mass in pp collisions at 14 TeV, and perform a two-dimensional study of xG in the M^2 and x plane.

4 Conclusion

We have reviewed the physics of non-linear QCD and high gluon densities at small fractional momenta x with emphasis on the existing data at HERA (proton) and RHIC (nucleus) which support the existence of a parton saturation regime (also known as colour-glass-condensate). The future perspectives at the LHC have been presented, including the promising capabilities of the forward CMS detectors to study the parton densities down to $x \sim 10^{-6}$ with various hard probes (jets, quarkonia, Drell-Yan). The programme of investigating the dynamics of low- x QCD is not only appealing in its own right but it is an essential prerequisite for predicting a large variety of hadron-, photon- and neutrino- scattering cross sections at very high energies.

Acknowledgments

The author acknowledges valuable comments from R. Vogt and J. Jalilian-Marian, and thanks J. Nystrand for providing the STARLIGHT photoproduction cross sections in PbPb at LHC. This work is supported by the 6th EU Framework Programme contract MEIF-CT-2005-025073.

References

1. M. Dittmar *et al.*, in *Proceeds. HERA and the LHC*, hep-ph/0511119.
2. V.N. Gribov and L.N. Lipatov, Sov. Journ. Nucl. Phys. **15** (1972) 438; G. Altarelli and G. Parisi, Nucl. Phys. **B126** (1977) 298; Yu. L. Dokshitzer, Sov. Phys. JETP **46** (1977) 641.
3. L.N. Lipatov, Sov. J. Nucl. Phys. **23** (1976) 338; E.A. Kuraev, L.N. Lipatov and V.S. Fadin, Zh. Eksp. Teor. Fiz. **72**, (1977) 3; Ya.Ya. Balitsky, L.N. Lipatov, Sov. J. Nucl. Phys. **28** (1978) 822.
4. S. Chekanov *et al.* [ZEUS Collab.], Phys. Lett. B **632** (2006) 13; A. Aktas *et al.* [H1 Collab.], Eur. Phys. J. C **46** (2006) 27.
5. C. Marquet and C. Royon, Nucl. Phys. B **739** (2006) 131.
6. C. Adloff *et al.* [H1 Collab.], Phys. Lett. B **520** (2001) 183.
7. E. Iancu, hep-ph/0608086.
8. D. Kharzeev and M. Nardi, Phys. Lett. B **507** (2001) 121; D. Kharzeev, E. Levin and M. Nardi, Nucl. Phys. A **747** (2005) 609.
9. See e.g. E. Iancu and R. Venugopalan, in *QGP*, Vol 3 Eds: R.C. Hwa and X.N. Wang, World Scientific, Singapore, hep-ph/0303204; J. Jalilian-Marian and Y. V. Kovchegov, Prog. Part. Nucl. Phys. **56** (2006) 104; and refs. therein.
10. J. Jalilian-Marian, A. Kovner, A. Leonidov and H. Weigert, Nucl. Phys. **B504** (1997) 415; Phys. Rev. **D59** (1999) 014014; E. Iancu, A. Leonidov and L. McLerran, Nucl. Phys. **A692** (2001) 583;
11. I. Balitsky, Nucl. Phys. **B** 463, (1996) 99; Yu.V. Kovchegov, Phys. Rev. **D 61**, (2000) 074018.
12. M. G. Ryskin *et al.*, Z. Phys. **C76**, (1997) 231.
13. T. Teubner, Proceedings. DIS'05, AIP Conf. Proc. **792** (2006) 416.
14. A. Accardi, nucl-th/0405046.
15. P. Newman, Int. J. Mod. Phys. A **19** (2004) 1061.
16. D. d'Enterria, J. Phys. G **30** (2004) S767.
17. A. Accardi *et al.*, in CERN Yellow report on *Hard probes in Heavy Ion collisions at the LHC*, hep-ph/0308248.
18. N. Armesto, J. Phys. G to appear, hep-ph/0604108.
19. K. Golec-Biernat and M. Wüsthoff, Phys. Rev. **D59**, (1999) 014017; Phys. Rev. **D60**, (1999) 114023.
20. J. R. Forshaw and G. Shaw, JHEP **0412** (2004) 052.
21. C. Marquet, L. Schoeffel, hep-ph/0606079.
22. E. Iancu, K. Itakura, L. McLerran, Nucl. Phys. **A708** (2002) 327.
23. K. J. Eskola, Nucl. Phys. A **698** (2002) 78.
24. N. Armesto, C. A. Salgado and U. A. Wiedemann, Phys. Rev. Lett. **94** (2005) 022002.
25. B. B. Back *et al.* [PHOBOS], Nucl. Phys. **A757** (2005) 28.
26. I. Arsene *et al.* [BRAHMS], Nucl. Phys. **A757** (2005) 1.
27. V. Guzey, M. Strikman, W. Vogelsang, Phys. Lett. B **603** (2004) 173
28. D. Kharzeev, Y. Kovchegov, K. Tuchin, Phys. Lett. B **599** (2004) 23
29. A. S. Ayan *et al.*, J. Phys. G **30** (2004) N33.
30. V. Berardi *et al.* [TOTEM], "TOTEM: Technical design report", CERN-LHCC-2004-002.
31. P. Katsas *et al.*, submitted to Nucl. Instrum. Methods A.
32. O. A. Grachov *et al.*, Proceedings. CALOR'06, nucl-ex/0608052.
33. A. H. Mueller and H. Navelet, Nucl. Phys. B **282** (1987) 727.
34. D. d'Enterria, Proceedings. *Quark Matter'05*, nucl-ex/0601001.
35. S. R. Klein, J. Nystrand, Phys. Rev. C **60** (1999) 014903; A. Baltz, S. Klein, J. Nystrand, Phys. Rev. Lett. **89** (2002) 012301.